scientific reports

Check for updates

OPEN

Comprehensive evaluation of the environmental performance and durability of biochar-incorporated concrete

Seung-Beom Kang[1], Jin-Seok Woo[2], Minkyeong Pyo[3], Hyun-Do Yun[2]✉ & Wonchang Choi[1]✉

To achieve global carbon neutrality, the construction industry is increasingly focused on reducing the carbon footprint of cement-based materials. However, comprehensive evaluations of biochar-incorporated concrete integrating long-term mechanical performance, freeze–thaw durability, and environmental impact remain limited. To address these issues, this study presents a comprehensive experimental evaluation of wood-based biochar as an alternative supplementary cementitious material (ASCM) in concrete. The physical characteristics of the biochar were analyzed using scanning electron microscopy (SEM), SEM–EDX, and Brunauer–Emmett–Teller (BET) analyses, and the chemical characteristics were evaluated using XPS. Concrete performance was evaluated in terms of mechanical properties (compressive strength, flexural strength, and static modulus), freeze–thaw durability with quantitative image-based surface analysis, and a life cycle assessment (LCA) was performed to quantify global warming potential (GWP). The results indicate that concrete containing 5% biochar achieved the target design strength of 24 MPa, whereas 7% replacement resulted in a compressive strength reduction of up to 35.5% compared to the plain mix. After 300 freeze–thaw cycles, the 5% biochar mixture maintained a durability factor of 96.8% and reduced the increase in surface scaling and increase in void count by approximately 74 and 72%, respectively, compared with the plain specimen. LCA results revealed that increasing the biochar replacement ratio reduced GWP, with up to a 27.7% reduction at 7% replacement. Considering both mechanical performance and environmental impact, a biochar replacement range of 3–5% was identified as optimal. These findings demonstrate that wood-based biochar is a viable ASCM for sustainable and low-carbon concrete construction.

Keywords Biochar, Compressive strength, Freeze–thaw, Environmental impact assessment

Major countries around the world are formulating and implementing policies to achieve carbon neutrality to address climate change. In 2019, the European Union announced the European Green Deal to achieve carbon neutrality by 2050[1]. The United States declared its plan to achieve zero carbon emissions in certain industrial sectors by 2035 and full carbon neutrality by 2050[2]. In addition, the United States plans to implement the Clean Competition Act[3], and the European Union intends to introduce the Carbon Border Adjustment Mechanism[4]. Accordingly, the Korean government announced the 2050 Carbon Neutrality Scenario and the 2030 Nationally Determined Contribution. These policies outline the need to reduce greenhouse gas emissions across major sectors, which include the construction industry, and to present corresponding strategies[5]. In the construction sector, key mitigation measures include the use of low-carbon building materials, improved energy efficiency, and the expansion of renewable energy adoption. Therefore, the development and application of low-carbon construction materials are essential to achieving decarbonization in the construction industry.

The cement industry accounts for approximately 7% to 8% of global carbon dioxide emissions, and thus, reducing carbon emissions during cement production has emerged as a critical challenge in achieving net-zero carbon targets[6]. Consequently, growing environmental concerns have highlighted biochar, a renewable resource derived from organic waste biomass, as a material of interest. Biochar is a porous carbonaceous material that is obtained by pyrolyzing biomass under oxygen-limited conditions, and it possesses excellent carbon sequestration

[1]Department of Architectural Engineering, Gachon University, Seongnam-Si 13120, Republic of Korea. [2]Department of Architectural Engineering, Chungnam National University, Daejeon 34134, Republic of Korea. [3]Department of Chemical and Biological Engineering, Gachon University, Seongnam-Si 13120, Republic of Korea. ✉email: wiseroad@cnu.ac.kr; wchoi@gachon.ac.kr

capability[7]. Although biochar has traditionally been utilized mainly as a soil amendment and adsorbent[8], recent studies have focused on employing biochar and similar novel materials as eco-friendly construction materials[9,10].

Studies that have investigated the incorporation of biochar into mortar to enhance the performance of cementitious materials have found that a replacement ratio of 2 to 5% by weight of cement can achieve comparable or improved performance of cement mortar[6,9,11–16]. Research also has examined the application of biochar in concrete. Owing to its high porosity and large specific surface area, biochar exhibits excellent water absorption capacity, which has been reported to enhance moisture retention and evaporative cooling performance when biochar is incorporated into pervious concrete[17]. Biochar also has been shown to reduce pore size within the concrete matrix and establish connections with hydration products, thereby helping to prevent early failure and contributing to the improvement of concrete's flexural strength[18].

A previous study that investigated the long-term performance of concrete containing biochar showed that the inclusion of 2 and 5% wood waste-based biochar by weight of cement, followed by two years of curing, resulted in improvements in both the compressive and flexural strength of the concrete[19]. Another study, in which biochar was substituted at levels of 2.5 to 10% and specimens were cured in air and water for one year, found that the mixture that contained 5% biochar exhibited the most favorable compressive and flexural performance of the concrete specimens tested[20]. Compared with plain concrete, the compressive strength of the concrete specimens with biochar increased by up to 25 percent. This improvement was attributed to the internal curing effect of the biochar and densification of the microstructure. These results indicate the potential applicability of biochar in structural concrete. However, research on cement-based materials incorporating biochar over extended periods remains significantly limited.

A study that evaluated the durability of concrete that contains biochar found that the inclusion of 2 to 4% biochar by mass of cement enhanced durability by densifying the concrete's microstructure and reducing permeability via the filler effect[21]. In addition, results from freeze–thaw resistance tests demonstrated that an appropriate amount of biochar in cement can reduce mass loss and surface scaling[22]. The pore structure of biochar has been reported to enhance the freeze–thaw resistance of concrete and reduce its permeability[23]. Another study has reported that, at relatively high biochar dosages, the porous structure and water absorptivity of biochar can lead to an increase in larger pore fractions in cementitious materials after freeze–thaw cycles. This finding indicates that an optimal dosage of biochar can act in a manner similar to an air-entraining agent within concrete, thereby improving its freeze–thaw resistance[24]. However, the effects of biochar incorporation on the durability of concrete, particularly with regard to the quantitative evaluation of concrete's deterioration under environmental conditions such as freeze–thaw cycles, remain insufficiently investigated.

Recent studies have shown that the mechanical performance of biochar-modified mortar depends on feedstock type and physicochemical characteristics, with wood-based biochar demonstrating more favorable strength performance than biochar with coarse particles and low specific surface area. Biochar incorporation can also alter fresh concrete behavior due to its high surface area and porous structure, influencing workability and hydration processes. Environmental assessments have reported a carbon sequestration potential of up to 9.40 kg CO_2 per cubic meter of concrete. Recent studies also suggest the need for improved understanding of long-term performance and highlight challenges related to standardization for the practical application of biochar in concrete[25,26].

According to ASTM C1709[27], an alternative supplementary cementitious material (ASCM) is defined as a material that contributes positively to the strength, durability, workability, or other performance characteristics of concrete or mortar. This ASCM category includes not only ground granulated blast furnace slag, fly ash, and silica fume, but also novel materials. For biochar to be utilized in practice and standardized in the construction industry, its applicability must be demonstrated through the material characterization and performance evaluation of concrete as specified in this standard. The performance evaluation of an ASCM requires material characterization as well as assessments of the material's mechanical properties and durability, including its compressive strength, flexural strength, modulus of elasticity, and freeze–thaw resistance. Under climatic conditions such as those in Korea, where freeze–thaw cycles occur repeatedly for approximately five months each year, the evaluation of freeze–thaw resistance should be considered thoroughly to ensure durability[28].

Previous studies have reported improvements in individual mechanical or durability properties. However, comprehensive evaluation of wood-based biochar as an ASCM at the concrete level under a standardized performance framework such as ASTM C1709 remains limited. This study aims to provide an integrated evaluation to support the practical feasibility of wood-based biochar as an ASCM at the concrete level. To this end, we prepared concrete containing biochar under large-scale mix conditions and with consideration of practical field applications, and evaluated its mechanical and durability properties. The physical and chemical characteristics of biochar were analyzed and established biochar replacement ratios by weight of cement. Subsequently, the mechanical performance was evaluated by measuring the compressive strength, flexural strength, and static modulus of elasticity over curing periods of up to 365 days. In addition, the freeze–thaw resistance was assessed in accordance with ASTM C666. The applicability of biochar in concrete based on the results of mechanical and durability performance tests were evaluated to suggest its applicability for use as an ASCM.

Experimental program

Materials and mix proportions

Ordinary Portland cement (OPC), classified as ASTM C150 Type I, was used in this study. The chemical composition of the cement was analyzed using X-ray fluorescence (XRF), and the major oxide components are presented in Table 1. To improve the workability of the concrete mixtures, a high-range water-reducing admixture was employed.

The biochar (WB) was produced through pyrolysis of wood pellet-based biomass at approximately 650 °C by Company K located in Daegu, Republic of Korea. To enable its use as an alternative supplementary cementitious

Type	SiO_2	Al_2O_3	CaO	MgO	SO_2	Fe_2O_3
OPC	22.1	5.0	63.8	1.6	2.0	3.0

Table 1. Chemical compositions of OPC (wt%).

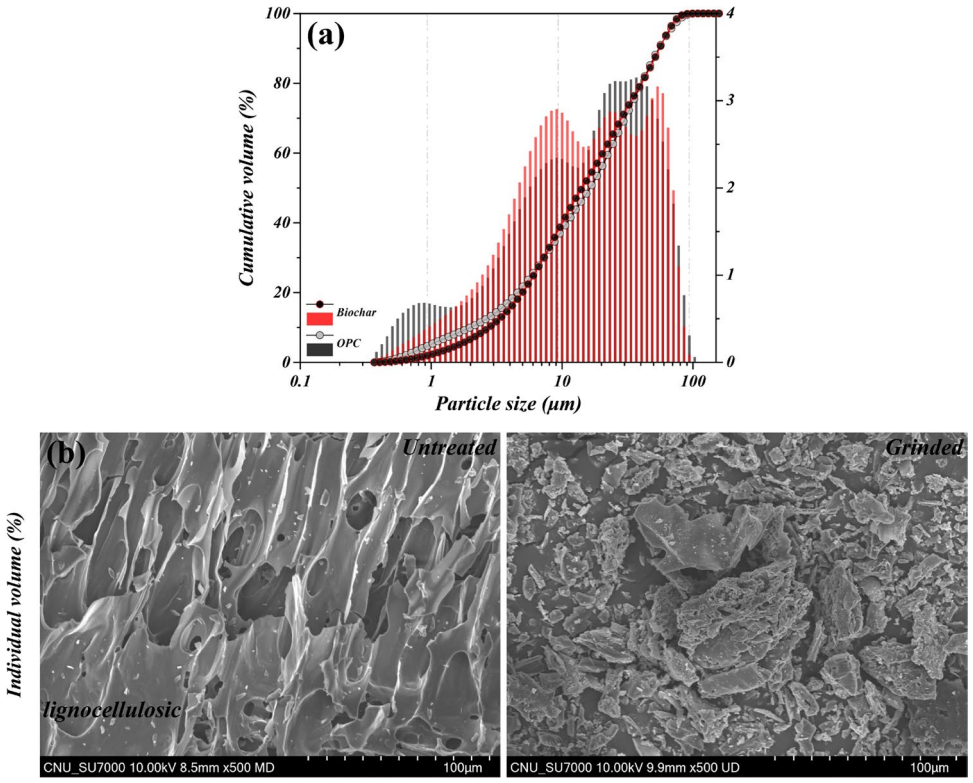

Fig. 1. (**a**) Comparison of particle size distribution between grinded Biochar and OPC; (**b**) porous surface microstructure of grinded WB.

Element composition	C	O	Na	Mg	Al	Si	S	Cl	K	Ca	Fe
WB	86.96	11.91	0.07	0.09	0.07	0.16	0.04	0.1	0.12	0.3	0.17

Table 2. Element Composition of WB.

material (ASCM), the biochar was oven-dried at 105 °C for 24 h and subsequently ground for more than 30 min using a roll mill at a rotational speed of 250–350 RPM.

The particle size characteristics of OPC and WB were analyzed using laser diffraction over a size range of 0.4–2000 μm, and the results are shown in Fig. 1a. The D10, D50, and D90 values of WB were 2.82, 14.51, and 56.71 μm, respectively, while those of OPC were 2.029, 16.70, and 55.98 μm. The average particle size was 22.64 μm for WB and 23.36 μm for OPC, indicating a similar particle size distribution with most particles smaller than 100 μm. These results suggest that WB possesses comparable fineness to OPC, supporting its potential applicability as an ASCM.

Despite undergoing mechanical grinding, the inherent porous structure of WB was preserved, while the initial large pores were substantially reduced, as observed in Fig. 1b. This indicates that the functional characteristics of the material were retained while the microstructural uniformity was improved[9]. According to the EDS analysis results presented in Table 2, the oxygen-to-carbon (O/C) ratio of WB was measured to be 0.10, which satisfies the commonly accepted threshold of 0.2 for chemically stable biochar[29]. Therefore, WB can be considered a promising material in terms of long-term stability and carbon sequestration potential.

The complete mix proportions are presented in Table 3. Four concrete mix designs were prepared for the experimental program, in which biochar (WB) was used to replace ordinary Portland cement (OPC) at replacement levels of 0, 3, 5, and 7% by weight. The concrete mixing was conducted using a full-scale batch plant system to simulate field production conditions. For all mixes, the target compressive strength was set at 24 MPa, and the air content was maintained at 4.5 ± 1.5%. According to previous studies, biochar exhibits high moisture

Type	W/B (%)	S/A (%)	Unit weight (kg/m^3)					
			W	C	S	G	Biochar	SP
Plain	50.0	40.0	165	330	712	1069	–	–
WB_3%				320			10	0.66
WB_5%				313.5			16.5	0.66
WB_7%				307			23	0.66

Table 3. Mix proportions. W/B is water-to-binder ratio, S/A is sand/aggregate ratio, C is cement, S is fine aggregate, G is coarse aggregate, SP is super plasticizer, WB is wood biochar.

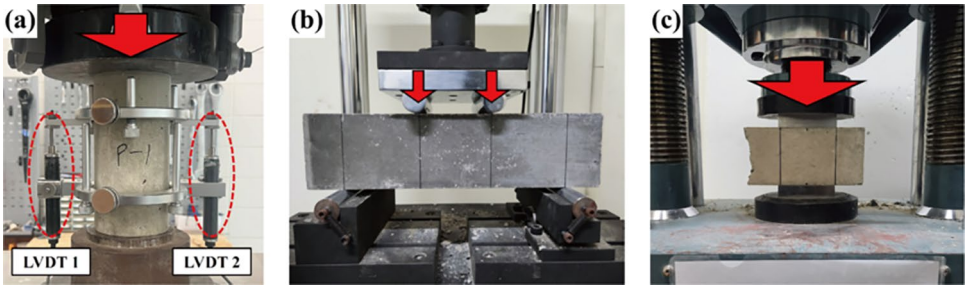

Fig. 2. Mechanical performance test set-ups: (**a**) compressive strength test; (**b**) flexural strength test; (**c**) flexural-compressive strength tested specimens.

absorption due to its porous structure, which can negatively affect the workability of concrete[9,19–21,30,31]. To mitigate this effect and ensure adequate flowability, a high-range water-reducing admixture was incorporated at a dosage of 0.2 wt% of cement in all mixtures.

The fresh concrete was cast into cylindrical molds (100 mm in diameter × 200 mm in height, 9 specimens per mix) and prismatic molds (100 mm × 100 mm × 400 mm, 9 specimens per mix). Initial curing was carried out under sealed conditions using plastic sheets to prevent moisture loss during early hydration.

Analysis of biochar properties

Various analytical techniques were employed to evaluate the physical properties of the ground WB. First, the microstructure and surface elemental composition of WB were examined using Scanning Electron Microscopy (SEM) coupled with Energy Dispersive Spectroscopy (EDS). Surface functional groups were analyzed using Fourier Transform Infrared Spectroscopy (FTIR, Bruker VERTEX 80v) within the frequency range of 4000–400 cm^{-1}. In addition, the surface chemical composition was assessed through X-ray Photoelectron Spectroscopy (XPS, Thermo Scientific, USA) utilizing Al Kα radiation. The porosity characteristics were evaluated using a Tristar II surface area analyzer by measuring nitrogen adsorption–desorption isotherms at liquid nitrogen temperature (77 K, – 196 °C). Based on these measurements, the Brunauer–Emmett–Teller (BET) method was applied to determine the specific surface area, and the Barrett–Joyner–Halenda (BJH) method was used to analyze the pore size distribution quantitatively. Furthermore, to obtain additional insights into the internal pore structure, mercury intrusion porosimetry (MIP) was performed using an Autopore porosimeter.

Biochar-concrete experimental program

All specimens were initially cured for 24 h under controlled conditions at 22 ± 3 °C and 60 ± 3% relative humidity. After demolding, the specimens were subjected to water curing for 28, 56, and 365 days at 20 ± 3 °C and 95 ± 5% relative humidity to minimize moisture loss.

For each mix, three cylindrical specimens were prepared for compressive strength testing at 28, 56, and 365 days. Three prismatic specimens per mix were tested for flexural strength at 28 and 56 days, and an additional three prismatic specimens were allocated for freeze–thaw resistance testing.

Compressive and flexural behaviors

Compressive strength and flexural strength were measured in accordance with ASTM C39[32] and ASTM C78[33], respectively. In particular, after the completion of freeze–thaw testing, each prismatic specimen was cut in half to evaluate both flexural and compressive strengths on the same specimen, thereby enabling a comparative analysis of strength variation due to freeze–thaw cycles. Figure 2 illustrates the overall experimental setup for mechanical performance testing.

Figure 2a shows the setup for the compressive strength test, in which a cylindrical specimen was instrumented with a compressive strain gauge to record the stress–strain behavior. The test was conducted using a hydraulic universal testing machine (UTM) with a maximum load capacity of 2000 kN, and the loading rate was controlled at 0.25 MPa/s ± 0.05 MPa/s. The static modulus of elasticity was calculated in accordance with ASTM C469[34].

Figure 2b illustrates the setup for the flexural strength test, conducted using the four-point bending method. A UTM with a maximum capacity of 100 kN was used, and the loading rate was set at 0.02 MPa/s. Following the flexural strength test, the specimen was repositioned between compression plates to evaluate flexural-compressive strength based on the Korean Standard KS F 2413[35]. The setup for this test is shown in Fig. 2c.

Freeze–thaw resistance of concrete

The freeze–thaw resistance was evaluated in accordance with Procedure B (rapid freezing in air and thawing in water) of ASTM C666[36]. Specimens were water-cured for 14 days prior to testing, as specified in the standard, and then subjected to up to 300 freeze–thaw cycles. Each cycle consisted of lowering the temperature from + 4 to − 18 °C, followed by thawing back to + 4 °C. The full cycle, including both freezing and thawing phases, was completed within 4 h.

During the freeze–thaw testing, the specimens were evaluated every 30 cycles for dynamic modulus of elasticity, mass, and surface condition. The dynamic modulus was measured using the transverse vibration method in accordance with ASTM C215[37]. Based on the measurements, the relative dynamic modulus of elasticity and durability factor were calculated using Eqs. (1), (2), and (3), respectively.

Figure 3 presents the overall test configuration. Figure 3a and b show the actual setup and schematic of the driving (K) and receiving (P) transducers used for dynamic modulus measurements, while Fig. 3c and d illustrate the freeze–thaw test equipment and the main testing conditions.

$$E_D = CMn^2 \tag{1}$$

where E_D is the dynamic Young's modulus of elasticity (MPa), M is the mass of the specimen (kg), and n is the fundamental transverse frequency (Hz). C is 0.9464 $(L^3T/bt^3)\cdot m^{-1}$ for a prism where L is the length of the specimen, m, t and b are the dimensions of the cross-section of a prism specimen m, t is the direction the specimen is driven, and T is the correction factor that depends on the ratio of the radius of gyration K (the radius of gyration for a prism is $t/3.464$).

$$P_c = E_1/E_0 \times 100 \tag{2}$$

where P_c is the relative dynamic modulus of elasticity after c cycles of freezing and thawing (%), E_1 is the dynamic modulus of elasticity after c cycles of freezing and thawing, and E_0 is the dynamic modulus of elasticity at 0 cycles of freezing and thawing.

$$DF = PN/M \tag{3}$$

where DF is the durability factor of the test specimen, P is the relative dynamic modulus of elasticity at N cycles (%), N is the number of cycles at which P reaches the specified minimum value for discontinuing the test or the specified number of cycles at which exposure is to be terminated, whichever is less, and M is the specified number of cycles at which exposure is to be terminated.

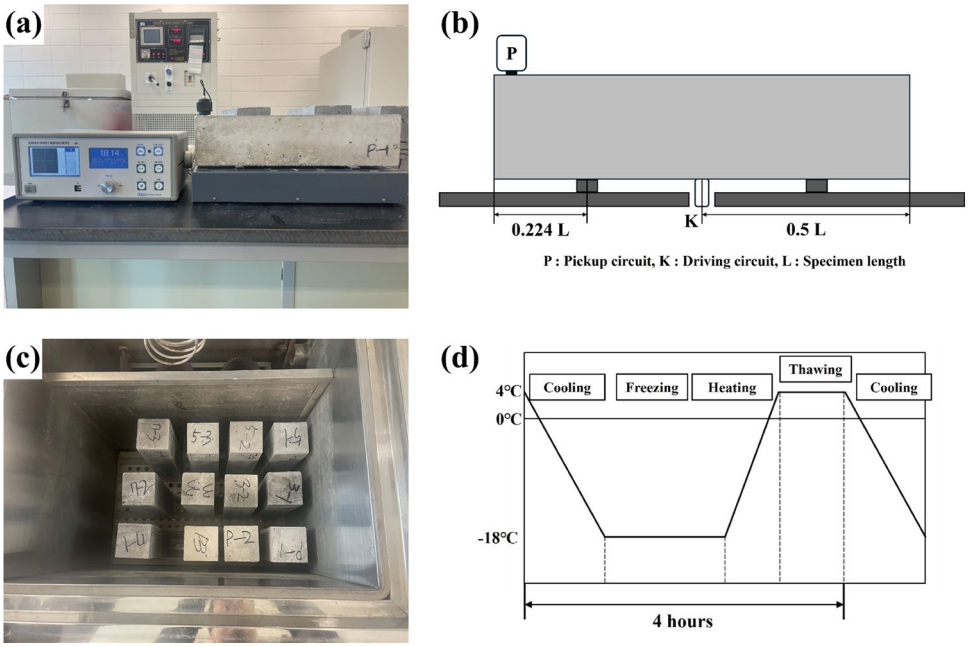

Fig. 3. Freeze–thaw test set-up: (**a**) dynamic elastic modulus measurement apparatus; (**b**) schematic diagram of dynamic elastic modulus test set-up; (**c**) freeze–thaw test specimens; (**d**) diagram of freeze–thaw test cycle.

Scanning electron microscopy
Small fragments collected from the specimens before and after freeze–thaw cycles were dried using silica gel. Subsequently, a thin platinum coating was applied to the surface of each specimen, and imaging was performed using a field emission scanning electron microscope (FE-SEM, SU7000, Hitachi, Japan) operated at an accelerating voltage of 10 keV.

Pore structure
The pore structure of the cement paste before and after freeze–thaw cycles was characterized using a mercury intrusion porosimeter (Autopore IV 9510). The applied pressure ranged from 0 to 600,000 psi (414 MPa).

Results and discussion

Physicochemical properties of biochar

To evaluate the surface characteristics and chemical reactivity of WB, FTIR and XPS analyses were conducted. The FTIR spectrum results are presented in Fig. 4a, where vibrational peaks corresponding to various functional groups were observed. A strong absorption band at 871 cm^{-1} corresponds to out-of-plane bending vibrations of aromatic C–H, indicating the presence of condensed aromatic domains formed during high-temperature gasification[38,39]. Such aromatic structures contribute to the durability and chemical stability of WB, potentially enhancing structural resilience in the highly alkaline environment of concrete. The peak near 1400 cm^{-1} is attributed to bending vibrations of CH and CO bonds and stretching of aromatic C = C, suggesting surface oxygen-containing functional groups that impart chemical reactivity to WB[40]. Peaks observed at 1587 cm^{-1} and 1700 cm^{-1} indicate the presence of conjugated carbonyl (C = O) groups, typically associated with carboxylic acids and aldehydes[38]. These groups may enhance early-stage reactivity via ion exchange or electrostatic interaction with cement hydration products.

Absorption bands detected in the 1980–2112 cm^{-1} range correspond to nitrile (C≡N) or alkyne (C≡C) functional groups, indicating increased surface unsaturation and potential redox activity, which may confer catalytic properties[39,41]. A peak near 2200 cm^{-1} is associated with cumulated double bonds or isocyanate (N = C = O) groups, reflecting possible chemical interactions within the cement matrix[42]. Moreover, the peak at 3700 cm^{-1} corresponds to O–H stretching vibrations from alcohol, phenol, or carboxylic acid-derived hydroxyl groups. These hydrophilic groups can promote water interaction and improve hydration uniformity[43,44]. The presence of diverse oxygen-containing functional groups suggests that WB may improve bonding and microstructural integration with cement hydration products through enhanced chemical reactivity and adsorption.

The XPS analysis results shown in Fig. 4b are consistent with the FTIR findings. The survey spectrum revealed that the dominant peak was C1s, confirming the carbon-based structure of WB. Simultaneously, various inorganic elements such as Ca, Si, K, and Mg were also detected, likely derived from ash constituents in the original biomass. These inorganic species can contribute to pH buffering, ion exchange, and secondary reactivity, thereby enhancing chemical durability and microstructural stability in concrete.

High-resolution fitting of the C1s peak indicated that oxygen-containing functional groups accounted for more than 85% of the total signal. In particular, the presence of C–O and O–C = O groups supports the potential for chelation and electrostatic interactions with metal ions and cement hydration products[45]. These XPS results align with the FTIR-determined functional groups and further support that WB has the material characteristics of a reactive filler or chemical promoter within the cement matrix.

The pore characteristics of WB were analyzed using nitrogen adsorption–desorption (BET) and mercury intrusion porosimetry (MIP). The BET isotherm, shown in Fig. 5a, exhibited a Type IV curve with an H4 hysteresis loop according to IUPAC classification, indicating a material with a combination of mesopores (2–50 nm) and micropores[46]. The BJH pore size distribution in Fig. 5b showed a peak in the 2–5 nm range, confirming a relatively uniform mesoporous structure.

The specific surface area, as measured by the Brunauer–Emmett–Teller (BET) method, was 49.19 m^2/g. Under relative pressure (P/P_0) conditions, the total pore volume for pores smaller than 371.77 nm in diameter was

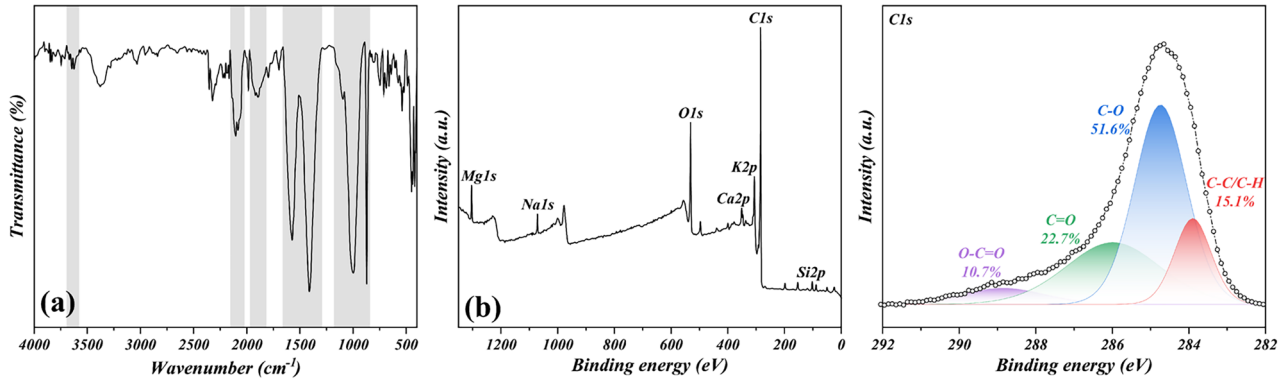

Fig. 4. FTIR and XPS spectra of WB: (**a**) FTIR spectra; (**b**) full scan and region scans of C 1 s and peak fitting results.

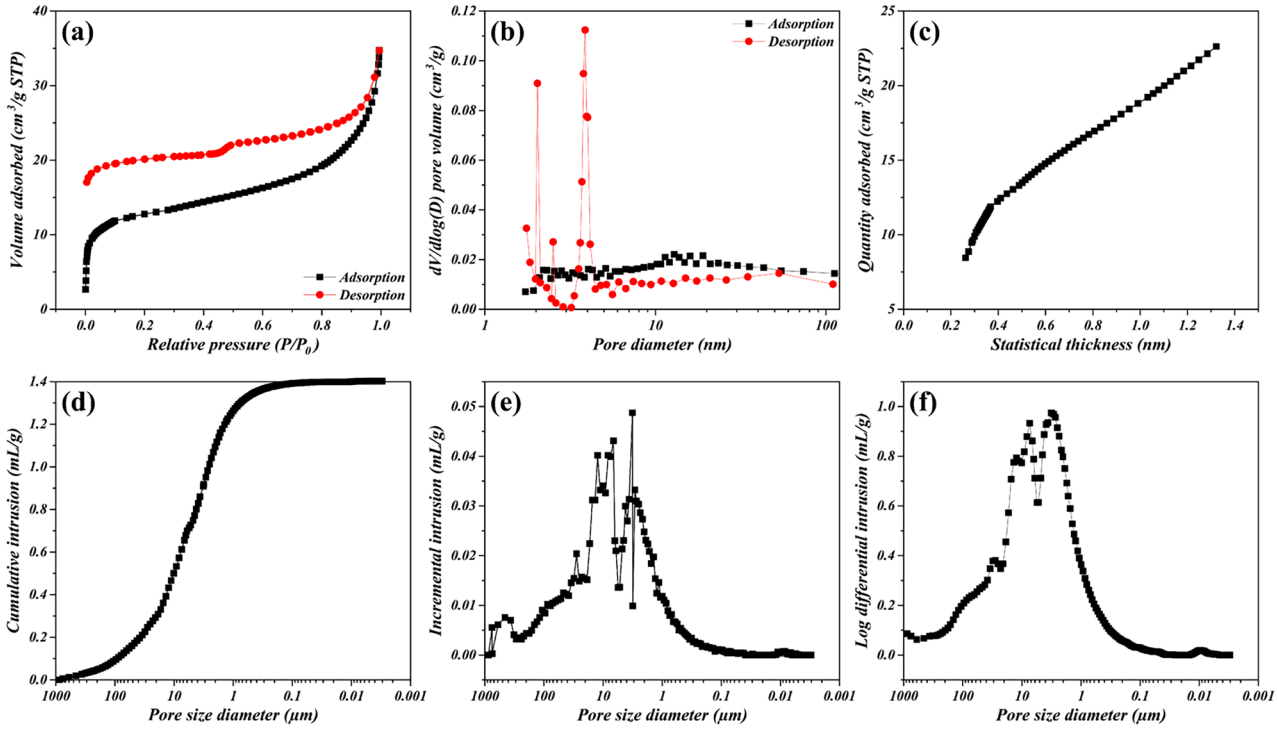

Fig. 5. BET and MIP analysis results of WB: (**a**–**c**) BET results; (**d**–**f**) MIP results.

0.05371 cm^3/g, and the average pore diameter was 9.78 nm. According to t-plot analysis in Fig. 5c, approximately 64% of the total surface area (31.67 m^2/g) originated from micropores, while the external surface area was measured at 17.51 m^2/g. These features indicate a favorable structure for reactivity and adsorption.

Meanwhile, the MIP results revealed larger pore structures not captured by BET analysis. The total pore volume was measured at 0.2929 cm^3/g, the average pore diameter was approximately 88.6 nm, and the porosity was calculated to be 30.64%. The mercury-intrusion-derived specific surface area was 1.323 m^2/g. The pore size distribution was concentrated in the 0.01–1 μm range, with a notable peak in the 0.1–0.2 μm interval, indicating a well-developed macroporous structure. These results indicate that WB possesses a hierarchical pore system comprising micropores, mesopores, and macropores.

According to Lehmann (2007) and Shafie et al. (2012), water retention is optimized when pore diameters are below 30 μm[7,47]. Therefore, the microporous and mesoporous structure of WB is considered to positively contribute to cement hydration by regulating water retention and release, thereby enhancing reactivity and strength development[12].

Compressive properties

Table 4 summarizes the compressive strength, ultimate strain, and elastic modulus of each specimen, while Fig. 6a–l illustrate the stress–strain curves at various curing ages. At 28 days, the Plain specimen exhibited the highest average compressive strength. In contrast, all WB-incorporated specimens showed a general reduction in strength, which can be attributed to the decreased cement content and the consequent limitation in hydration product formation due to partial replacement with biochar[48].

In terms of replacement ratio, compressive strength was relatively maintained at 3–5%, whereas a significant decline was observed at the 7% replacement level. This trend aligns with the commonly reported threshold level of approximately 5%, below which the beneficial microstructural effects of biochar can offset strength losses. Beyond this level, however, increased porosity dominates, leading to notable strength reductions[49]. The limited strength reduction at replacement levels below 5% can be explained by the packing effect of fine biochar particles, which reduces porosity and increases the overall density of the mixture[50,51]. In addition, internal curing facilitated by the moisture retained within the biochar may promote continued hydration and contribute to microstructural densification[52,53]. Both WB_3% and WB_5% specimens exceeded the target compressive strength of 24 MPa, and a small strength gain was observed in all mixes beyond 56 days. At one year, the Plain specimen showed a strength increase of approximately 19% compared to its 28-day value, while WB_3% and WB_5% exhibited gains of 14% and 13%, respectively. These results indicate that continued hydration and long-term strength development are feasible even in the presence of biochar[54,55]. On the other hand, the WB_7% mix consistently demonstrated the lowest compressive strength at all ages, with a maximum reduction of approximately 35.5% compared to the Plain mix. This significant decline is likely due to the excessive replacement of cement, which disrupts paste continuity and hinders the formation of calcium silicate hydrate (C–S–H) gel, thereby compromising mechanical integrity.

Specimen	Compressive strength (MPa)	Peak strain (mm/mm)	Elastic modulus (GPa)
Plain (28 days)	30.16 ± 0.37	0.00225 ± 0.000108	21.2 ± 2.64
Plain (56 days)	31.24 ± 1.40	0.00216 ± 0.000068	22.6 ± 0.09
Plain (1 year)	35.93 ± 0.22	0.00262 ± 0.000046	21.7 ± 0.48
WB_3% (28 days)	26.06 ± 1.52	0.00217 ± 0.000268	20.9 ± 1.38
WB_3% (56 days)	26.43 ± 2.29	0.00198 ± 0.000284	21.2 ± 0.29
WB_3% (1 year)	29.84 ± 1.19	0.00224 ± 0.000022	23.9 ± 0.95
WB_5% (28 days)	26.55 ± 0.65	0.00210 ± 0.000282	20.4 ± 0.84
WB_5% (56 days)	27.53 ± 1.62	0.00238 ± 0.000070	20.2 ± 0.14
WB_5% (1 year)	30.12 ± 1.65	0.00213 ± 0.000460	25.8 ± 2.99
WB_7% (28 days)	19.46 ± 1.13	0.00245 ± 0.000394	18.5 ± 1.32
WB_7% (56 days)	21.87 ± 1.58	0.00198 ± 0.000448	19.6 ± 0.65
WB_7% (1 year)	23.09 ± 0.37	0.00213 ± 0.000383	22.5 ± 0.50

Table 4. Compressive strength test results.

The modulus of elasticity was calculated in accordance with ASTM C469. At 28 days, the Plain specimen exhibited the highest modulus. A gradual decrease in modulus was observed with increasing biochar replacement levels. For WB_3% and WB_5%, the modulus was reduced by less than 5% compared to the Plain specimen. At 56 days, the reductions ranged from approximately 6 to 11%, while the WB_7% specimen exhibited a consistent reduction of around 13% at both 28 and 56 days[56]. Overall, when the replacement level remained at or below 5%, the reduction in elastic modulus was limited, suggesting minimal adverse effects on mechanical performance at early ages[15]. Changes in the modulus of elasticity with curing age varied between mixes. While the plain specimen showed a decrease in modulus over time, likely due to accumulated microcracks, the biochar-containing specimens demonstrated an increasing trend. At one year, the modulus of elasticity for WB_3%, WB_5%, and WB_7% specimens increased by approximately 10, 19, and 4%, respectively, compared to the plain mix. This implies that biochar particles may initially act as stress-dissipating inclusions. Over the long term, internal curing and continued hydration may contribute to sustained stiffness development[56,57]. These mechanisms should be verified through further microstructural investigation in future studies.

Crack patterns

Figure 7 illustrates the failure patterns of concrete specimens at different curing ages, with the primary crack paths indicated by red lines. The observed crack patterns varied depending on the curing duration and biochar replacement ratio. In the Plain specimens, failure was primarily characterized by inclined or X-shaped shear cracks, which are indicative of a typical brittle and shear failure mode under uniaxial compression[58,59]. These cracks propagated diagonally across the specimen, reflecting localized and concentrated fracture behavior. In contrast, the WB_3% and WB_5% specimens exhibited crack patterns predominantly aligned parallel to the loading direction, resembling axial splitting rather than shear failure. These vertical cracks were distributed more uniformly along the height of the specimens, suggesting a delayed localization of shear failure and a transition toward a more distributed fracture mode.

For the WB_7% specimens, a mixture of vertical and inclined cracks was observed across all curing periods, with irregular crack orientations and multiple concurrent failure paths. This behavior corresponds with the overall reductions in compressive strength and elastic modulus reported in Table 4, reflecting a deterioration in structural coherence due to excessive biochar content. Overall, the inclusion of biochar significantly influenced the axial compressive failure behavior of concrete, shifting the dominant failure mode from localized shear to more distributed splitting or mixed-mode cracking. This indicates that biochar alters the internal stress distribution and crack propagation mechanisms in concrete, thereby delaying fracture localization and promoting more varied failure patterns[56,60].

Flexural properties

Figure 8a presents the results of the flexural strength tests. At a curing age of 28 days, both the Plain and WB_5% specimens exhibited an average flexural strength of 3.9 MPa, whereas the WB_3% and WB_7% specimens showed relatively lower values of 3.3 and 3.15 MPa, respectively. At 56 days, the WB_5% specimen achieved the highest flexural strength of 4.4 MPa, while the WB_7% specimen consistently exhibited the lowest flexural strength at all curing ages[13].

This behavior indicates a biochar incorporation level of 5% within the concrete matrix, thereby enhancing the mechanical interlocking between biochar particles and the hydrated cement matrix and delaying the initiation of early-stage cracking. It is well established that flexural strength is strongly influenced by the size and spatial distribution of macropores within the cross-section[61], with smaller and more uniformly distributed pores generally leading to improved flexural performance. From this perspective, a 5% biochar content is considered to refine the pore structure and contribute to flexural strength enhancement, whereas excessive biochar incorporation at 7% likely induces a non-uniform pore structure, resulting in a reduction in flexural strength.

For most specimens, the flexural strength after freeze–thaw cycles showed a slight increase compared to that at 28 days. This trend suggests that the strength gain associated with continued cement hydration during the testing period outweighed the micro-damage induced by repeated freeze–thaw actions[62]. However, even after

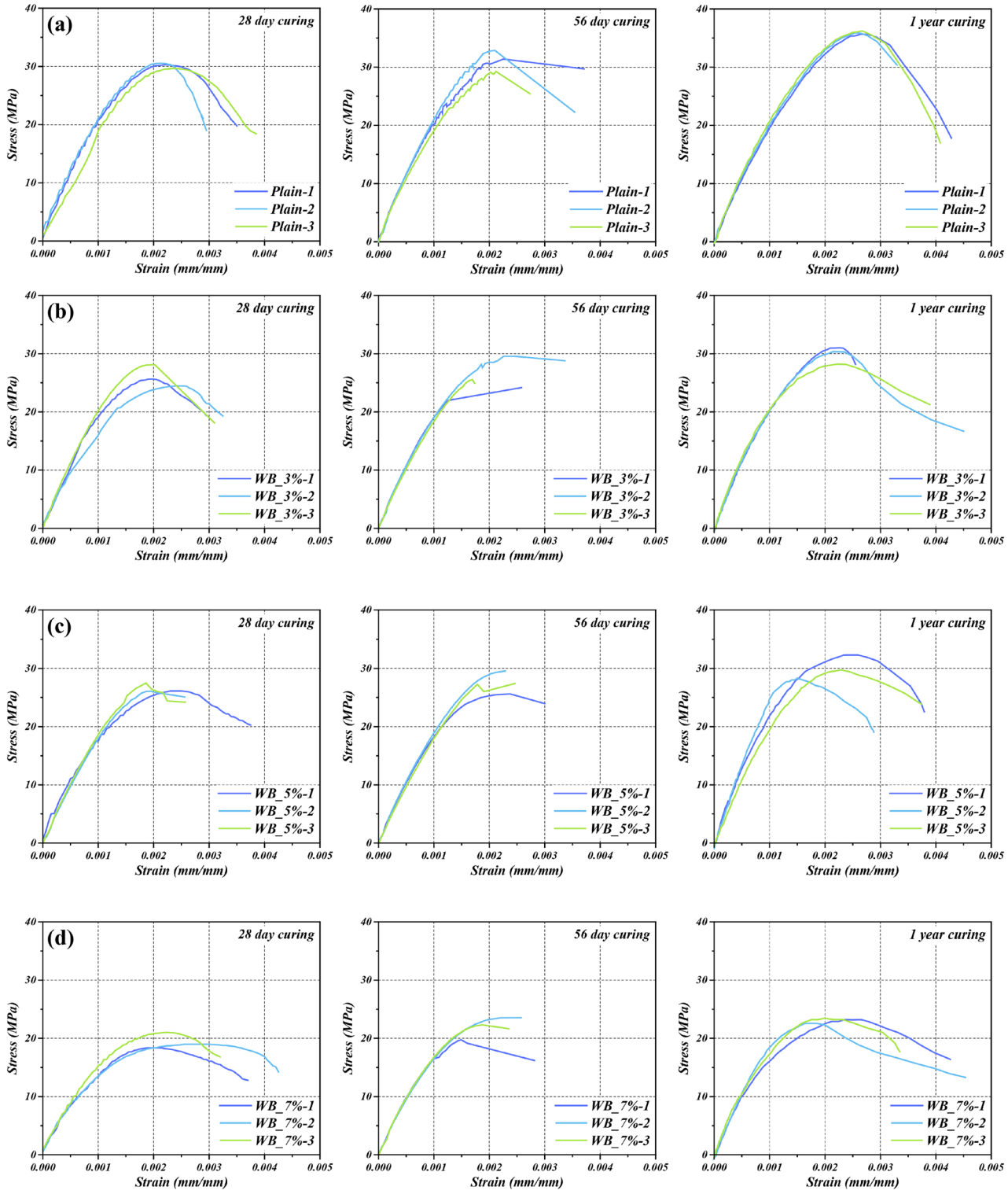

Fig. 6. Stress–strain curves: (**a**) Plain; (**b**) WB_3%; (**c**) WB_5%; (**d**) WB_7%.

freeze–thaw exposure, the WB_7% specimen exhibited the lowest flexural strength, which may be attributed to the formation of additional pores near the tensile zone at high biochar content. These pores are likely to promote stress concentration under bending loads, thereby leading to a deterioration in flexural performance[12].

Figure 8b presents the results of the residual compressive strength tests conducted on prism specimens after the flexural strength tests. At curing ages of 28 and 56 days, the WB_5% specimens exhibited compressive strength levels comparable to those of the Plain specimens. After exposure to freeze–thaw cycles, the compressive strength of the WB_5% specimens decreased by approximately 8% relative to the 28-day strength, which was

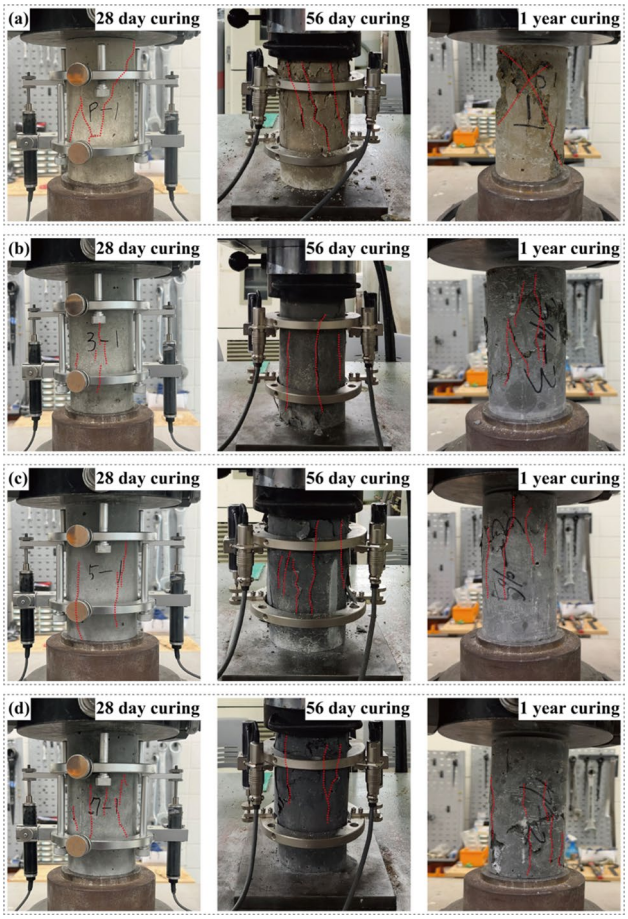

Fig. 7. Crack patterns: (**a**) Plain; (**b**) WB_3%; (**c**) WB_5%; (**d**) WB_7%.

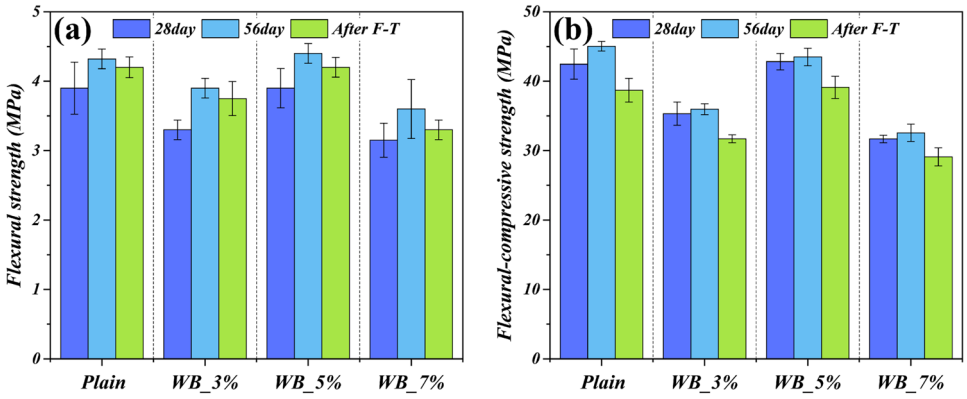

Fig. 8. (**a**) Flexural strength; (**b**) Flexural-compressive strength.

nearly identical to the reduction observed in the Plain specimens. In contrast, the WB_3% specimens showed a strength reduction of approximately 10% after freeze–thaw exposure, while the WB_7% specimens exhibited a reduction of about 8%.

Overall, no significant differences in the residual flexural-compressive strength were observed with increasing biochar replacement ratio. The specimens incorporating 5% biochar maintained compressive performance comparable to that of the plain specimens, which can be attributed to the effective internal curing effect provided by biochar. In contrast, the specimens with 7% biochar content exhibited the lowest compressive strength, likely due to the combined effects of freeze–thaw damage and excessive pore formation. The observed trends in flexural-compressive strength exhibit a similar tendency to those obtained from the compressive strength tests conducted on cylindrical specimens.

Freeze–thaw durability of concrete specimens

Figure 9a–d illustrate the variation in relative dynamic elastic modulus (RDEM) with the number of freeze–thaw cycles. Among the Plain specimens, the second specimen failed after 60 cycles and was therefore excluded from subsequent analysis. All mixes retained over 90% of their initial RDEM after 300 cycles, indicating that all mixtures tested in this study exhibited excellent freeze–thaw resistance. The WB_3% and WB_5% specimens showed degradation patterns similar to the Plain mix, while the WB_7% specimen exhibited a relatively sharp decline in RDEM after 150 cycles. This behavior is likely due to increased interfacial weakness between the cement matrix and biochar particles at higher replacement levels, making the composite more susceptible to microcracking under repeated freeze–thaw stress. In addition, the high moisture retention capacity of biochar is believed to play a key role in this deterioration. Water retained within the biochar may freeze during the cooling phase, generating internal expansion stresses that promote interfacial cracking and enlargement of capillary pores[24].

This trend is more clearly demonstrated by the durability factor (DF) values presented in Fig. 9e. A DF below 60% typically indicates poor freeze–thaw resistance. However, all specimens in this study recorded DF values above 90%, confirming their high durability. Specifically, the DF for the Plain specimen was 96.7%, while the WB_5% specimen recorded a slightly higher value of 96.8%, suggesting that an appropriate amount of biochar can even enhance freeze–thaw durability. This improvement may be attributed to the ability of biochar to act

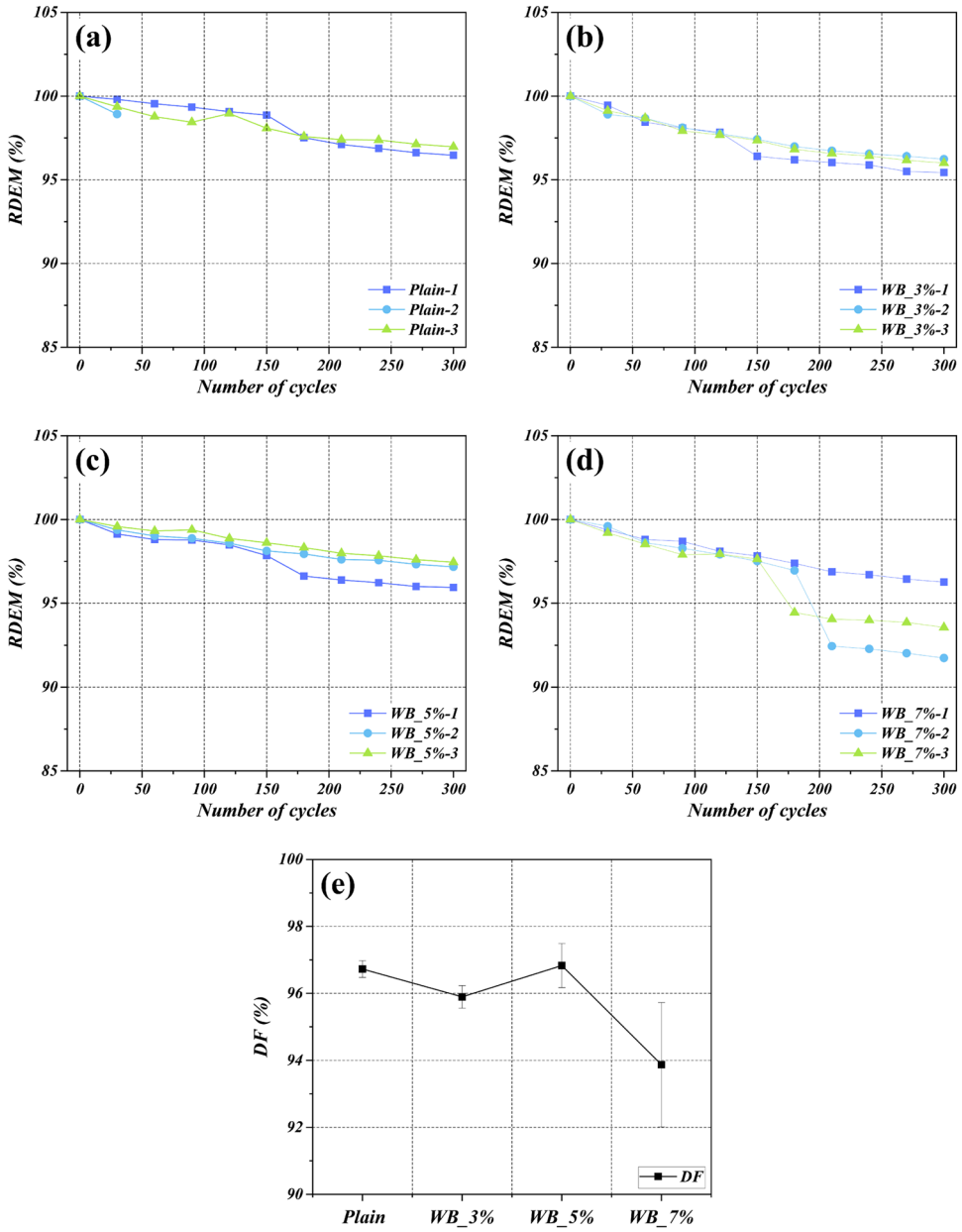

Fig. 9. RDEM and DF of specimens during freeze–thaw cycles: (**a**) RDEM of Plain; (**b**) RDEM of WB_3%; (**c**) RDEM of WB_5%; (**d**) RDEM of WB_7%; (**e**) DF.

similarly to air-entraining agents by introducing fine, well-dispersed pores that help mitigate internal pressure from ice formation[23]. Conversely, the DF of the WB_7% specimen decreased to 93.9%, which may result from exceeding the threshold replacement level—leading to weakened interfacial bonding and moisture-induced damage mechanisms.

Figure 10a–d present the mass loss ratios of specimens after 300 freeze–thaw cycles. The Plain specimen exhibited the lowest mass loss at 1.63%, while the specimens containing biochar generally showed increased mass loss. The WB_3% and WB_7% specimen recorded relatively higher losses of 2.77 and 2.78%, respectively. In contrast, the WB_5% specimen showed a mass loss of 2.03%, which was comparable to that of the Plain specimen.

These results indicate that while the inclusion of biochar may moderately reduce freeze–thaw resistance in terms of mass loss. Considering environmental sustainability as well, the use of biochar at levels up to 5% appears to be practically acceptable in terms of freeze–thaw durability performance. Furthermore, a correlation analysis between the DF and mass loss ratio revealed a clear trend: specimens with lower mass loss tended to exhibit higher durability factors.

Surface analysis after freeze–thaw

The surfaces of the specimens before and after freeze–thaw cycling (0 and 300 cycles) were quantitatively analyzed to evaluate the occurrence of surface scaling and pore formation. Using a Python-based image analysis program, deteriorated regions were extracted based on pixel filtering, followed by object separation. Surface scaling and voids were classified according to object area, where regions larger than 50 were defined as scaling and smaller regions as surface voids. Subsequently, an automatic object detection function was used to count the number of occurrences of each feature, and average values were calculated for each condition.

Image analysis was conducted on the exposed faces, excluding the casting surface, under identical imaging conditions. Figure 11 visually illustrates the entire procedure of the surface scaling and void analysis, while Table 5 summarizes the surface images and quantitative results obtained before and after freeze–thaw cycling. To enable a comparative evaluation of surface degradation due to freeze–thaw exposure, the increase rates of surface scaling and void formation were calculated using Eq. (4). This approach provided an objective basis for assessing the impact of repeated freeze–thaw cycles on surface deterioration.

$$Increaseratio\,(\%) = ((X_{300} - X_0)/X_0) \times 100 \tag{4}$$

where X_{300} is the number of surface voids or scaling instances detected after 300 freeze–thaw cycles, and X_0 is the number of surface voids or scaling instances detected before the freeze–thaw test.

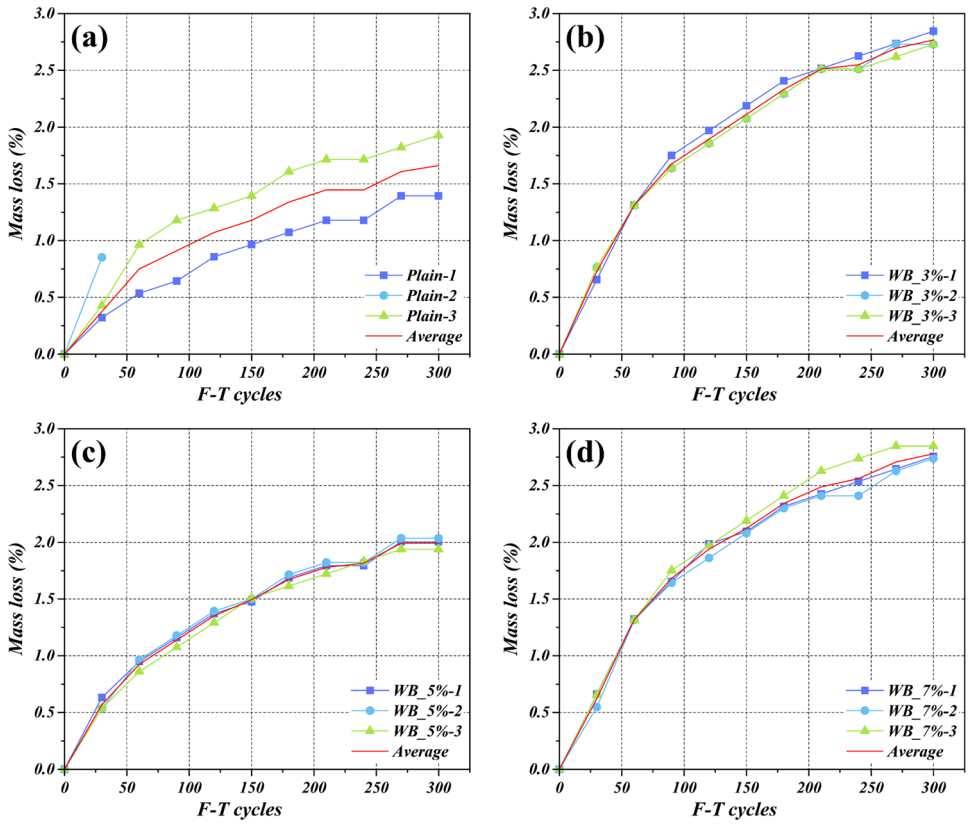

Fig. 10. Mass loss of specimens during freeze–thaw cycles.

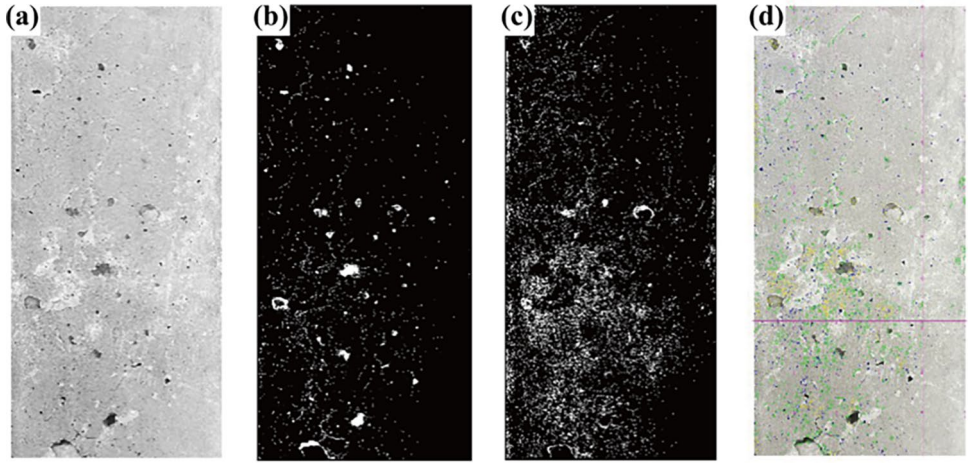

Fig. 11. Surface scaling and void analysis procedure: (**a**) surface image visualization; (**b**) void detection; (**c**) scaling detection; (**d**) measurement of surface void and scaling defects.

Figure 12a presents the mass loss, along with the average number of surface scaling events and void counts before and after 300 freeze–thaw cycles, while Fig. 12b visualizes the rate of increase in surface defects as a function of biochar replacement ratio. Under the initial (0-cycle) condition, the Plain specimen exhibited the fewest instances of surface scaling and void formation, and these metrics increased progressively with higher biochar content. However, after 300 cycles, the rate of increase in surface defects was significantly lower for the biochar-incorporated specimens compared to the Plain specimen. Specifically, the Plain specimen exhibited a 174.6% increase in scaling events and a 282.6% increase in void count, whereas the WB_3% specimen showed increases of 45.9 and 145.5%, WB_5% exhibited 45.8 and 78.5%, and WB_7% showed only 24.5 and 47.1%, respectively. These trends indicate that although specimens with higher biochar content initially exhibit more surface defects, the progression of surface degradation due to freeze–thaw cycling is effectively mitigated.

The reduced increase rates in scaling and void formation can be attributed to enhanced crack resistance imparted by biochar, which helps suppress surface deterioration[22,24]. The porous structure of biochar provides expansion space for freezing water, thereby dissipating internal stresses and delaying degradation progression[63]. This study found that the correlation between mass loss and surface degradation indicators was not consistent across all conditions. This implies that biochar affects both macroscopic durability and microstructural surface behavior in a complex manner. Overall, the WB_5% mix demonstrated stable performance across multiple durability indicators—including mechanical strength, mass loss rate, durability factor, and the rate of increase in surface defects. These results suggest that when used as an ASCM, biochar can improve durability, provided the replacement ratio is appropriately controlled.

Micro and pore structure analysis after freeze–thaw

Figure 13a presents the pore structure of the concrete specimens before freeze–thaw cycling. Compared to the Plain specimen, those incorporating biochar showed a reduction in the volume fraction of large pores. The WB_3% and WB_5% specimens exhibited porosity reductions of 8.78 and 22.05%, respectively, whereas the WB_7% specimen showed a 31.1% increase. These results suggest that biochar at a 5% replacement level contributes to matrix densification through micro-filler effects and internal curing. at 7% replacement, the increased porosity can be attributed to the reduced cement content and weakened biochar–cement interfacial bonding. Figure 13b shows the pore structure after 300 freeze–thaw cycles. An overall increase in porosity was observed across all mixes, with biochar-modified specimens showing an increase in pore volume. This is likely due to interfacial cracking and the formation of defects along the biochar–cement interface during cyclic freeze–thaw exposure. The marked growth in large pore volume suggests that freezing-induced expansion of water retained in the biochar pores caused interfacial cracking and coarsening of pores.

Figure 14 displays SEM images of the specimens prior to freeze–thaw cycling. SEM analysis can provide qualitative microstructural evidence of interfacial conditions and pore characteristics in cement-based materials[64]. Except for localized interfacial gaps, the biochar–cement interface exhibited relatively continuous contact between the biochar particles and surrounding hydration products. Hydration products were observed within the internal pores of the biochar, suggesting precipitation and physical filling of hydration phases within the porous structure. Such observations are consistent with the interaction between biochar surfaces and cement hydration products, which may contribute to the formation of C–S–H, CH, and AFm phases[65]. While hydration product deposition was also visible in the WB_3% specimen, it was less pronounced than in WB_5%. This behavior is considered to result from the combined effects of enhanced internal curing through water absorption and release by biochar at a 5% replacement level, together with an increased total surface area that provides additional nucleation sites for hydration products[66].

Figure 15 shows the microstructural features after freeze–thaw cycling. In most specimens, the interfacial transition zone (ITZ) between biochar and the cement matrix widened compared to the pre-cycling state. This

ID		0 cycle	300 cycles
Plain	Surface imaging		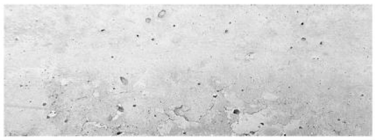
	Analysis results	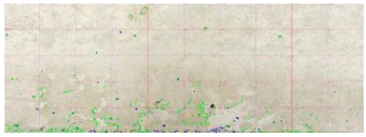	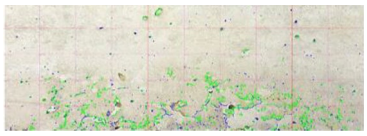
WB_3%	Surface imaging	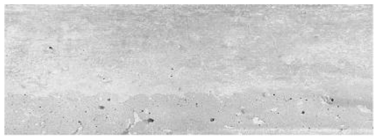	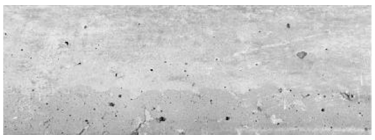
	Analysis results	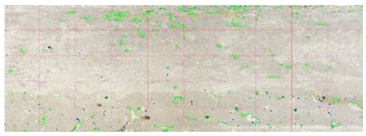	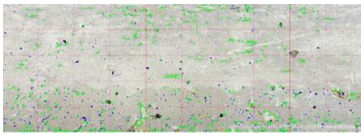
WB_5%	Surface imaging	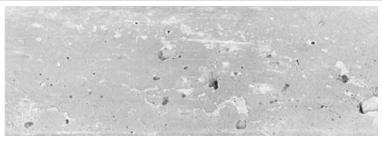	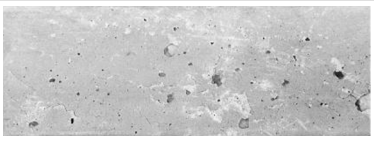
	Analysis results	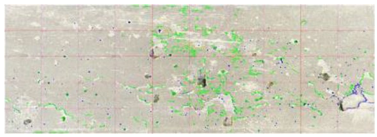	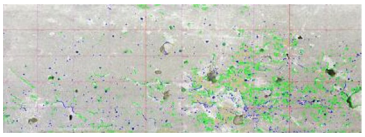
WB_7%	Surface imaging	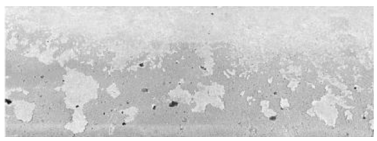	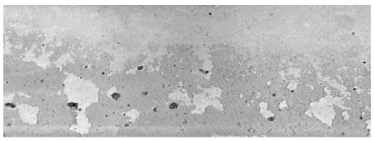
	Analysis results	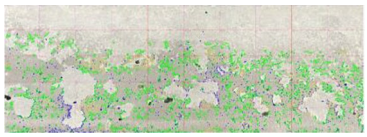	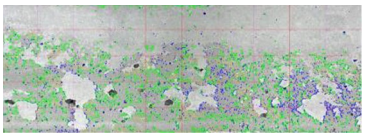

Table 5. Surface image analysis of specimens before and after freeze–thaw cycles.

degradation may be attributed to increased CH concentrations in the ITZ and dilution effects caused by water released from the biochar. Furthermore, the expansion of water absorbed in the biochar during freezing likely generated local stresses, leading to interfacial cracking. The WB_3% and WB_5% specimens exhibited relatively fewer cracks and voids compared to WB_7%. This supports the interpretation that, at low replacement levels, biochar can act similarly to an air-entraining agent, improving freeze–thaw resistance. In the WB_7% specimens, continuity in the cementitious matrix is compromised, and interfacial vulnerability becomes dominant, resulting in microstructural deterioration that is considered to have been accelerated. Previous studies have also combined SEM observations with EDS-based compositional analysis to interpret hydration products and microstructures in blended cementitious systems, and future studies are recommended to include quantitative evaluation of ITZ thickness and elemental distribution[67].

Environmental impact assessment

To quantitatively assess the sustainability of concrete specimens incorporating biochar, a life cycle assessment (LCA) was conducted. The system boundary was defined as cradle-to-gate, covering stages A1–A3, from raw material extraction to the factory gate. The analysis focused primarily on environmental burdens arising from raw material production and composite manufacturing, which are the major contributors to variation among the mixes. Environmental impact factors per kilogram of material were obtained from Environmental Product Declarations (EPDs) and relevant literature sources. A summary of these values is presented in Table 6, while Table 7 shows the calculated environmental impacts and cost per unit volume (1 m^3), based on the standard mix

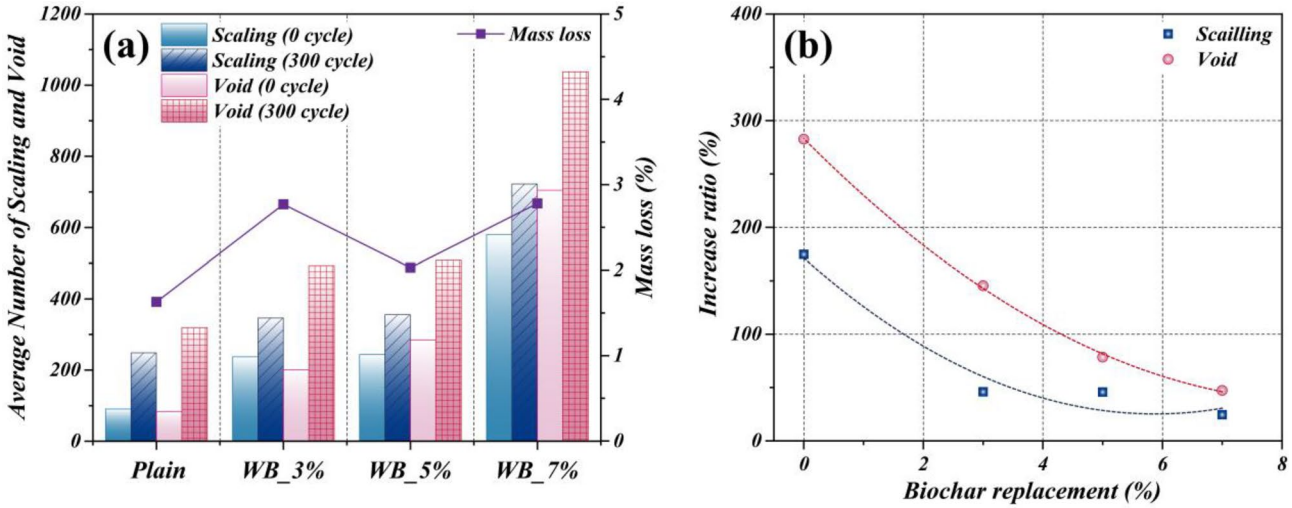

Fig. 12. Surface analysis: (**a**) number of scaling instances and voids; (**b**) increase ratios of scaling instances and voids.

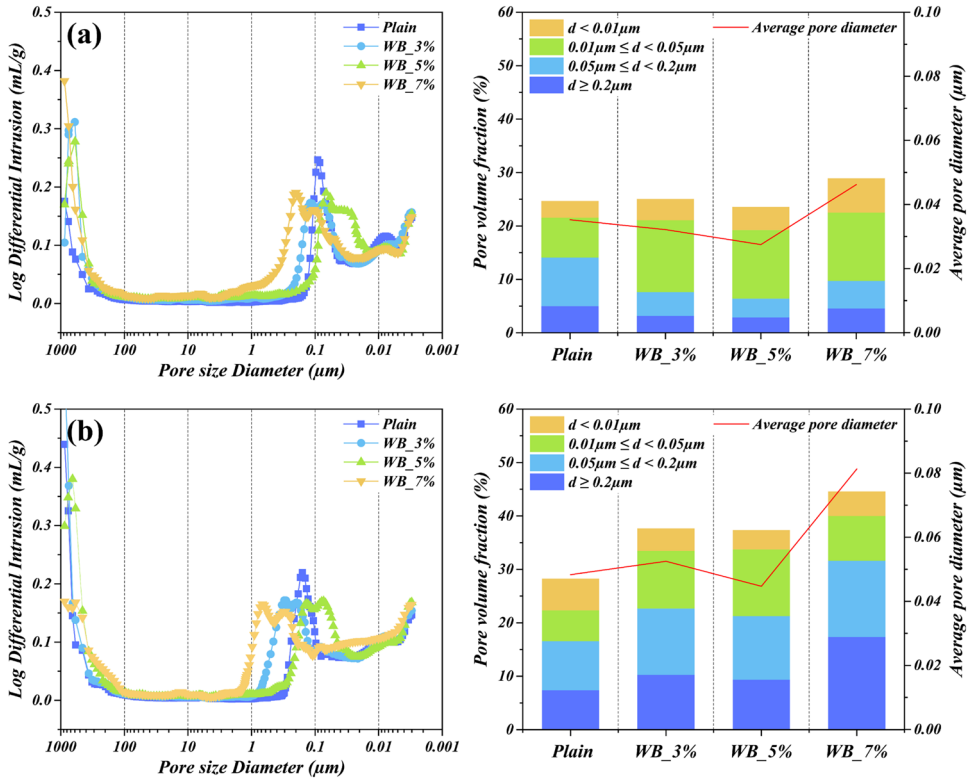

Fig. 13. Pore structure of specimens before and after freeze–thaw cycles: (**a**) Plain; (**b**) WB_3%; (**c**) WB_5%; (**d**) WB_7%.

proportions provided in Table 3. The environmental impacts were calculated by directly applying the unit impact factors from EPDs to the material quantities of each mixture.

The selected indicators for evaluation were Global Warming Potential (GWP) and Primary Energy Non-Renewable Total (PENRT), and the analysis was performed in accordance with ISO 14040 and ISO 14044 standards[68,69]. Figure 16 illustrates the normalized comparison of environmental impacts and costs for each mix design. The results showed a consistent reduction in GWP with increasing biochar replacement, with the WB_7% mix achieving a 27.7% lower GWP compared to the Plain mix. This is attributed to the carbon-sequestering nature of biochar, which possesses negative GWP values.

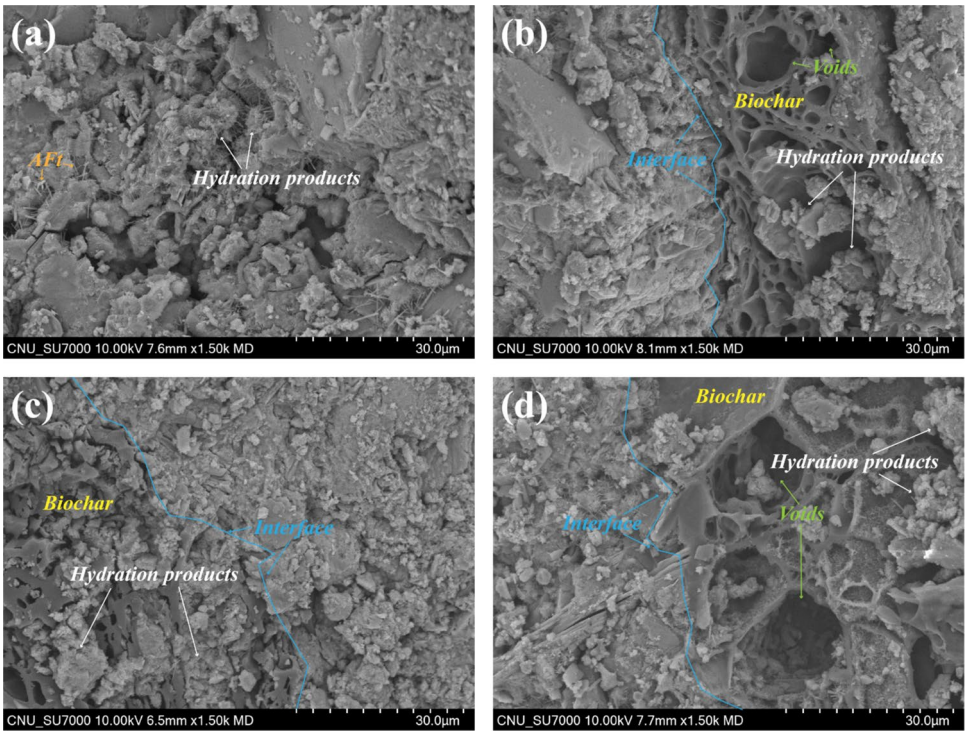

Fig. 14. SEM images of biochar-concrete ITZ before freeze–thaw cycles: (**a**) Plain; (**b**) WB_3%; (**c**) WB_5%; (**d**) WB_7%.

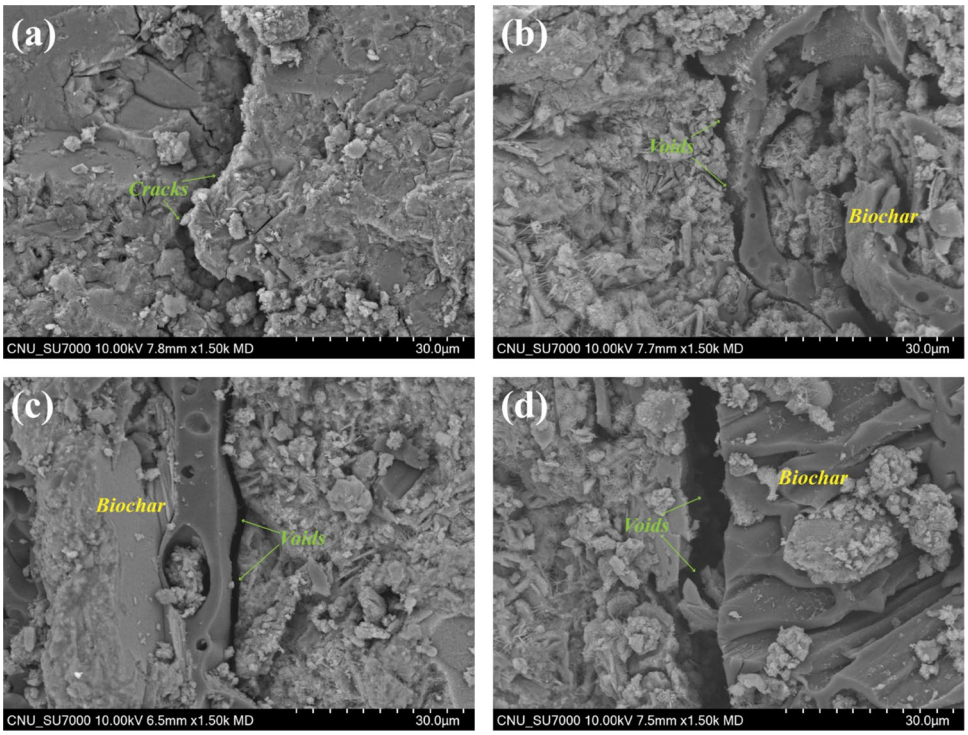

Fig. 15. SEM images of biochar-concrete ITZ after freeze–thaw cycles: (**a**) Plain; (**b**) WB_3%; (**c**) WB_5%; (**d**) WB_7%.

Material	Data source	GWP (kg CO_2 eq/kg)	PENRT(MJ/kg)
Cement	UltraTech Cement Ltd. (2022)[70]	0.996	5.96
Sand	Vilniaus Karjerai, JSC. (2021)[71]	0.000928	0.0126
Gravel			
Biochar	Biokolprodukter AB. (2024)[72]	-3.03	1.05
Super plasticizer	Sika Services AG. (2023)[73]	0.896	20.1
Water	Nienborg et al. (2018)[74]	0.01	0.06

Table 6. Impact categories per kg of cementitious materials. Biochar incorporated into concrete is assumed to create a permanent carbon sink with no downstream carbon emissions[72].

Specimen	GWP (kg CO_2 eq)	PENRT (MJ)
Plain	331.98	1999.14
WB_3%	292.29	1963.31
WB_5%	266.13	1931.39
WB_7%	239.96	1899.48

Table 7. Environmental impact per unit volume (1 m^3) of cementitious concrete mixtures.

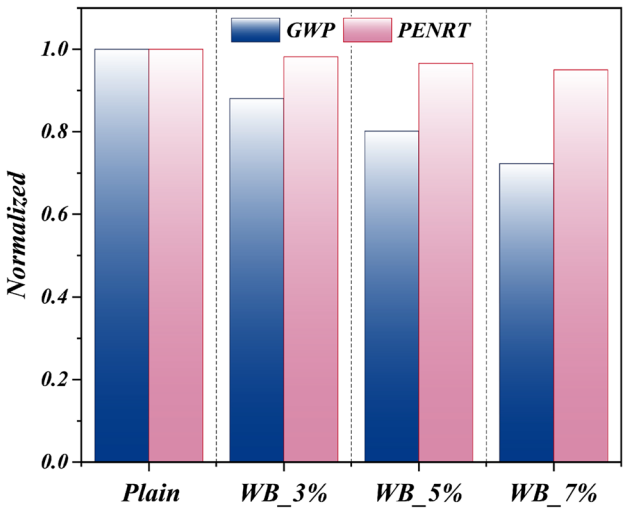

Fig. 16. Normalized GWP and PENRT of concrete mixtures.

PENRT exhibited a gradual decline as the replacement ratio increased, which can be explained by the relatively low energy input required during the pyrolysis process used for biochar production. These findings suggest that biochar can substantially enhance the environmental performance of cement-based composites. Considering the balance between environmental benefits and mechanical performance, the optimal replacement ratio range appears to be between 3 and 5%.

The environmental assessment performed in this study focused on the material production stage within a cradle-to-gate scope. Given the enhanced freeze–thaw durability observed, potential reductions in maintenance frequency and associated environmental impacts during the service period may be expected; however, these effects were not quantified here. A more comprehensive sustainability evaluation would require the inclusion of full life-cycle stages in future studies.

Conclusions

We evaluated concrete incorporating domestically produced wood-based biochar to assess its applicability as an ASCM in terms of material properties, mechanical performance, freeze–thaw resistance, and environmental impact. The conclusions are as follows.

1. The material characterization showed that wood-based biochar has a PSD comparable to cement, along with a porous structure and high specific surface area confirmed by BET and MIP analyses. Its high carbon content and low O/C ratio indicate chemical stability and long-term carbon sequestration potential.

2. The evaluation of mechanical performance and durability showed that concrete with 5% biochar replacement provided stable compressive strength, flexural strength, and freeze–thaw resistance, maintaining durability factors above 90% after freeze–thaw cycles. However, replacement levels exceeding 5% resulted in reductions in compressive strength and elastic modulus.
3. The surface deterioration analysis showed that although the initial number of surface voids increased with higher biochar content, the increase rates of scaling and void formation after 300 freeze–thaw cycles decreased in the biochar-incorporated mixtures. This trend suggests that the porous structure of biochar can provide space for water expansion and mitigate the progression of surface deterioration during freeze–thaw exposure.
4. The environmental impact assessment of GWP and PENRT showed that greenhouse gas emissions could be reduced by up to 27.7% depending on the biochar replacement ratio. Considering both mechanical performance and environmental impact, a replacement level of 3–5% is appropriate for concrete applications. Therefore, biochar is regarded as a material with high potential for applicability as an ASCM in concrete.

For future studies, it is recommended to conduct detailed quantitative analyses of the mechanisms of strength development and to evaluate performance at structural member dimensions for practical applications.

Data availability

The original contributions presented in the study are included in the article, further inquiries can be directed to the corresponding author/s.

Received: 27 January 2026; Accepted: 23 March 2026
Published online: 28 March 2026

References

1. Kim, B. C. & Shin, E. C. Analysis of the EU Green Deal and Just Transition Mechanism: A focus on the implementation of the Just Transition Fund Regulation. *Korean J. Soc. Sci.* **42**(3), 215–249. https://doi.org/10.18284/jss.2023.12.42.3.215 (2023).
2. Fam, A. & Fam, S. Review of the US 2050 long term strategy to reach net zero carbon emissions. *Energy Rep.* **12**, 845–860. https://doi.org/10.1016/j.egyr.2024.06.031 (2024).
3. Li, D., Shen, B. & Siqin, T. Resource shuffling in global supply chains under the Clean Competition Act. *Transp. Res. E Logist. Transp. Rev.* **187**, 103591. https://doi.org/10.1016/j.tre.2024.103591 (2024).
4. Kumar, S., Gangotra, A. & Barnard, M. Towards a net zero cement: Strategic policies and systems thinking for a low-carbon future.. *Curr. Sustain. Renew. Energy Rep.* **12**(1), 5. https://doi.org/10.1007/s40518-025-00253-0 (2025).
5. Park, N. B. Comparative analysis and implications of studies on Korea's 2050 carbon-neutral scenario. *J. Clim. Change Res.* **13**(5), 689–704. https://doi.org/10.15531/KSCCR.2022.13.5.689 (2022).
6. Zhou, Z., Wang, J., Tan, K. & Chen, Y. Enhancing biochar impact on the mechanical properties of cement-based mortar: An optimization study using response surface methodology for particle size and content.. *Sustainability* **15**(20), 14787. https://doi.org/10.3390/su152014787 (2023).
7. Lehmann, J. A handful of carbon.. *Nature* **447**(7141), 143–144. https://doi.org/10.1038/447143a (2007).
8. Weber, K. & Quicker, P. Properties of biochar. *Fuel* **217**, 240–261. https://doi.org/10.1016/j.fuel.2017.12.054 (2018).
9. Han, S. & Choi, W. Evaluation of the mechanical properties of cement mortar containing wood-based bio-char.. *J. Korea Concr. Inst.* **35**(3), 285–292. https://doi.org/10.4334/JKCI.2023.35.3.285 (2023).
10. Bhatia, S. K. et al. Trends in renewable energy production employing biomass-based biochar.. *Bioresour. Technol.* **340**, 125644. https://doi.org/10.1016/j.biortech.2021.125644 (2021).
11. Choi, W. C., Yun, H. D. & Lee, J. Y. Mechanical properties of mortar containing bio-char from pyrolysis. *J. Korea Inst. Struct. Maintenance Inspect. (J. Korea Inst. Struct. Mai)* **16**(3), 67–74 (2012).
12. Gupta, S. & Kua, H. W. Effect of water entrainment by pre-soaked biochar particles on strength and permeability of cement mortar.. *Constr. Build. Mater.* **159**, 107–125. https://doi.org/10.1016/j.conbuildmat.2017.10.095 (2018).
13. Maljaee, H. et al. Effect of cement partial substitution by waste-based biochar in mortars properties. *Constr. Build. Mater.* **301**, 124074. https://doi.org/10.1016/j.conbuildmat.2021.124074 (2021).
14. Zeidabadi, Z. A., Bakhtiari, S., Abbaslou, H. & Ghanizadeh, A. R. Synthesis, characterization and evaluation of biochar from agricultural waste biomass for use in building materials. *Constr. Build. Mater.* **181**, 301–308. https://doi.org/10.1016/j.conbuildmat.2018.05.271 (2018).
15. Gupta, S., Kua, H. W. & Koh, H. J. Application of biochar from food and wood waste as green admixture for cement mortar. *Sci. Total Environ.* **619**, 419–435. https://doi.org/10.1016/j.scitotenv.2017.11.044 (2018).
16. Aziz, M. A. et al. Mechanical, non-destructive, and thermal characterization of biochar-based mortar composite. *Biomass Convers. Biorefinery* https://doi.org/10.1007/s13399-023-03838-1 (2023).
17. Tan, K. et al. Biochar from waste biomass as hygroscopic filler for pervious concrete to improve evaporative cooling performance. *Constr. Build. Mater.* **287**, 123078. https://doi.org/10.1016/j.conbuildmat.2021.123078 (2021).
18. Akhtar, A. & Sarmah, A. K. Novel biochar-concrete composites: Manufacturing, characterization and evaluation of the mechanical properties. *Sci. Total Environ.* **616**, 408–416. https://doi.org/10.1016/j.scitotenv.2017.10.319 (2018).
19. Sirico, A. et al. Effects of biochar addition on long-term behavior of concrete. *Theor. Appl. Fract. Mech.* **122**, 103626. https://doi.org/10.1016/j.tafmec.2022.103626 (2022).
20. Sirico, A. et al. Biochar from wood waste as additive for structural concrete. *Constr. Build. Mater.* **303**, 124500. https://doi.org/10.1016/j.conbuildmat.2021.124500 (2021).
21. Aneja, A., Sharma, R. L. & Singh, H. Mechanical and durability properties of biochar concrete. *Mater. Today Proc.* **65**, 3724–3730. https://doi.org/10.1016/j.matpr.2022.06.371 (2022).
22. Wang, L. et al. Application of nanotechnology in cementitious materials for enhanced concrete construction through carbon incorporation. *Carbon Lett.* **35**(2), 539–552. https://doi.org/10.1007/s42823-024-00792-4 (2025).
23. Murali, G. & Wong, L. S. A comprehensive review of biochar-modified concrete: Mechanical performance and microstructural insights. *Constr. Build. Mater.* **425**, 135986. https://doi.org/10.1016/j.conbuildmat.2024.135986 (2024).
24. Chen, T. et al. Effect of biochar characteristics on freeze-thaw durability of biochar-cement composites. *J. Build. Eng.* **102**, 111959. https://doi.org/10.1016/j.jobe.2025.111959 (2025).
25. Kang, S. B., Yun, H. D. & Choi, W. Feasibility on diverse biochars as supplementary cementitious materials. *Sci. Rep.* **15**(1), 40732. https://doi.org/10.1038/s41598-025-24618-z (2025).
26. Zhou, Y., Wang, S. & Chen, L. Progress and prospects of biochar as concrete filler: A review. *Alex. Eng. J.* **128**, 306–323. https://doi.org/10.1016/j.aej.2025.05.077 (2025).

27. ASTM C1709; Standard Guide for Evaluation of Alternative Supplementary Cementitious Materials (ASCM) for Use in Concrete. (ASTM International, 2018).
28. Kim, S. W., Lee, D. J., Kim, K. M. & Kim, J. S. An experimental study on the performance of RC beam according to the rapid freezing and thawing test method in the air. *J. Korea Inst. Struct. Maint. Insp.* **25**(4), 46–55. https://doi.org/10.11112/jksmi.2021.25.4.46 (2021).
29. Spokas, K. A. Review of the stability of biochar in soils: Predictability of O: C molar ratios. *Carbon Manag.* **1**(2), 289–303. https://doi.org/10.4155/cmt.10.32 (2010).
30. Suarez-Riera, D. et al. The effect of different biochar on the mechanical properties of cement-pastes and mortars. *Buildings* **13**(12), 2900. https://doi.org/10.3390/buildings13122900 (2023).
31. Gupta, S. & Kua, H. W. Carbonaceous micro-filler for cement: Effect of particle size and dosage of biochar on fresh and hardened properties of cement mortar. *Sci. Total Environ.* **662**, 952–962. https://doi.org/10.1016/j.scitotenv.2019.01.269 (2019).
32. ASTM C39; Standard Test Method for Compressive Strength of Cylindrical Concrete Specimens. (ASTM International, 2024).
33. ASTM C78; Standard Test Method for Flexural Strength of Concrete (Using Simple Beam with Third-Point Loading). (ASTM International, 2022).
34. ASTM C 469; Standard Test Method for Static Modulus of Elasticity and Poisson's Ratio of Concrete in Compression. (ASTM International, 2021).
35. KS F 2413; Standard test method for compressive strength of concrete after flexural strength test. (Korean Standards Association, 2020).
36. ASTM C 666; Standard Test Method for Resistance of Concrete to Rapid Freezing and Thawing. (ASTM International, 2015).
37. ASTM C 215; Standard Test Method for Fundamental Transverse, Longitudinal, and Torsional Resonant Frequencies of Concrete Specimens. (ASTM International, 2021).
38. Michalak, I., Baśladyńska, S., Mokrzycki, J. & Rutkowski, P. Biochar from a freshwater macroalga as a potential biosorbent for wastewater treatment. *Water* **11**(7), 1390. https://doi.org/10.3390/w11071390 (2019).
39. Moradi-Choghamarani, F., Moosavi, A. A. & Baghernejad, M. Determining organo-chemical composition of sugarcane bagasse-derived biochar as a function of pyrolysis temperature using proximate and Fourier transform infrared analyses. *J. Therm. Anal. Calorim.* **138**(1), 331–342. https://doi.org/10.1007/s10973-019-08186-9 (2019).
40. Beć, K. B., Grabska, J., Badzoka, J. & Huck, C. W. Spectra-structure correlations in NIR region of polymers from quantum chemical calculations. The cases of aromatic ring, C= O, C≡ N and C-Cl functionalities. *Spectrochim. Acta A Mol. Biomol. Spectrosc.* **262**, 120085. https://doi.org/10.1016/j.saa.2021.120085 (2021).
41. Li, B. et al. Enhanced adsorption capacity of tetracycline on tea waste biochar with KHCO3 activation from aqueous solution. *Environ. Sci. Pollut. Res.* **28**(32), 44140–44151. https://doi.org/10.1007/s11356-021-13817-6 (2021).
42. Ganesan, K., Guin, B., Wilbanks, E. & Sternberg, J. Synthesis and characterization of soy hull biochar-based flexible polyurethane foam composites. *Materials* **18**(9), 2006. https://doi.org/10.3390/ma18092006 (2025).
43. Yang, C. X., Zhu, Q., Dong, W. P., Fan, Y. Q. & Wang, W. L. Preparation and characterization of phosphoric acid-modified biochar nanomaterials with highly efficient adsorption and photodegradation ability. *Langmuir* **37**(30), 9253–9263 (2021).
44. Wang, Z. et al. Characterization of acid-aged biochar and its ammonium adsorption in an aqueous solution. *Materials* **13**(10), 2270. https://doi.org/10.3390/ma13102270 (2020).
45. Zhang, J., Ye, H., Gao, X. & Wu, W. Adsorption and desorption of polycarboxylate ether superplasticizer in fresh cementitious materials blended with mineral admixtures. *J. Mater. Res. Technol.* **17**, 1740–1751. https://doi.org/10.1016/j.jmrt.2022.01.145 (2022).
46. Thommes, M. et al. Physisorption of gases, with special reference to the evaluation of surface area and pore size distribution (IUPAC technical report). *Pure Appl. Chem.* **87**(9–10), 1051–1069. https://doi.org/10.1515/pac-2014-1117 (2015).
47. Shafie, S. T., Salleh, M. M., Hang, L. L., Rahman, M. & Ghani, W. A. W. A. K. Effect of pyrolysis temperature on the biochar nutrient and water retention capacity. *J. Purity Util. React. Environ.* **1**(6), 293–307 (2012).
48. Liu, W., Li, K. & Xu, S. Utilizing bamboo biochar in cement mortar as a bio-modifier to improve the compressive strength and crack-resistance fracture ability. *Constr. Build. Mater.* **327**, 126917. https://doi.org/10.1016/j.conbuildmat.2022.126917 (2022).
49. Tan, K., Pang, X., Qin, Y. & Wang, J. Properties of cement mortar containing pulverized biochar pyrolyzed at different temperatures. *Constr. Build. Mater.* **263**, 120616. https://doi.org/10.1016/j.conbuildmat.2020.120616 (2020).
50. Gupta, S., Kua, H. W. & Dai Pang, S. Biochar-mortar composite: Manufacturing, evaluation of physical properties and economic viability. *Constr. Build. Mater.* **167**, 874–889. https://doi.org/10.1016/j.conbuildmat.2018.02.104 (2018).
51. Gupta, S., Kua, H. W. & Dai Pang, S. Effect of biochar on mechanical and permeability properties of concrete exposed to elevated temperature. *Constr. Build. Mater.* **234**, 117338. https://doi.org/10.1016/j.conbuildmat.2019.117338 (2020).
52. Ahmad, S., Khushnood, R. A., Jagdale, P., Tulliani, J. M. & Ferro, G. A. High performance self-consolidating cementitious composites by using micro carbonized bamboo particles. *Mater. Des.* **76**, 223–229. https://doi.org/10.1016/j.matdes.2015.03.048 (2015).
53. Dixit, A., Gupta, S., Dai Pang, S. & Kua, H. W. Waste valorisation using biochar for cement replacement and internal curing in ultra-high performance concrete. *J. Clean. Prod.* **238**, 117876. https://doi.org/10.1016/j.jclepro.2019.117876 (2019).
54. Uddin, M. A. et al. The effect of curing time on compressive strength of composite cement concrete. *Appl. Mech. Mater.* **204**, 4105–4109. https://doi.org/10.4028/www.scientific.net/AMM.204-208.4105 (2012).
55. Sokołowska, J. J. Long-term compressive strength of polymer concrete-like composites with various fillers. *Materials* **13**(5), 1207. https://doi.org/10.3390/ma13051207 (2020).
56. Li, M. et al. Progressive development of cracks in biochar–cement composites through multiscale analysis. *Comput. Aided Civ. Infrastruct. Eng.* **40**(30), 5952–5971. https://doi.org/10.1111/mice.70090 (2025).
57. Rodier, L., Bilba, K., Onésippe, C. & Arsène, M. A. Utilization of bio-chars from sugarcane bagasse pyrolysis in cement-based composites. *Ind. Crops Prod.* **141**, 111731. https://doi.org/10.1016/j.indcrop.2019.111731 (2019).
58. Ahmad, J. et al. A review on failure modes and cracking behaviors of polypropylene fibers reinforced concrete. *Buildings* **12**(11), 1951. https://doi.org/10.3390/buildings12111951 (2022).
59. Dong, W., Huang, Y., Lehane, B., Aslani, F. & Ma, G. Mechanical and electrical properties of concrete incorporating an iron-particle contained nano-graphite by-product. *Constr. Build. Mater.* **270**, 121377. https://doi.org/10.1016/j.conbuildmat.2020.121377 (2021).
60. Li, M., Zhu, X., Zhang, Y. & Tsang, D. C. A multi-phase mechanical model of biochar–cement composites at the mesoscale. *Comput. Aided Civ. Infrastruct. Eng.* **39**(23), 3552–3572. https://doi.org/10.1111/mice.13307 (2024).
61. Snoeck, D., Schaubroeck, D., Dubruel, P. & De Belie, N. Effect of high amounts of superabsorbent polymers and additional water on the workability, microstructure and strength of mortars with a water-to-cement ratio of 0.50. *Constr. Build. Mater.* **72**, 148–157. https://doi.org/10.1016/j.conbuildmat.2014.09.012 (2014).
62. Lee, S. T., Park, S. H., Kim, D. G. & Kang, J. M. Effect of freeze–thaw cycles on the performance of concrete containing water-cooled and air-cooled slag. *Appl. Sci.* **11**(16), 7291. https://doi.org/10.3390/app11167291 (2021).
63. Sikora, P. et al. A systematic experimental study on biochar-cementitious composites: Towards carbon sequestration. *Ind. Crops Prod.* **184**, 115103. https://doi.org/10.1016/j.indcrop.2022.115103 (2022).
64. Chen, H., Liang, K., Chow, C. L. & Lau, D. Enhancing the engineering performance of lightweight limestone calcined clay cement concrete using used engine oil as a foam stabilizer. *J. Build. Eng.* **95**, 110187. https://doi.org/10.1016/j.jobe.2024.110187 (2024).

65. Xu, W. et al. Using waste to improve the weak: Recycled seashell as an ideal way to regulate the interfacial transition zone in biochar-cement composites. *Constr. Build. Mater.* **444**, 137765. https://doi.org/10.1016/j.conbuildmat.2024.137765 (2024).
66. Kallimani, R. & Minde, P. Investigation on combined use of biochar and ground granulated blast furnace slag as a supplementary admixture in concrete. *Environ. Sci. Pollut. Res.* **32**(13), 8201–8218. https://doi.org/10.1007/s11356-025-36210-z (2025).
67. Chen, H. & Yang, J. A new supplementary cementitious material: Walnut shell ash. *Constr. Build. Mater.* **408**, 133852. https://doi.org/10.1016/j.conbuildmat.2023.133852 (2023).
68. Arvanitoyannis, I. S. ISO 14040: life cycle assessment (LCA)–principles and guidelines. Waste management for the food industries, 97–132. (2008).
69. Standard, I. *Environmental Management-Life cycle Assessment-Requirements and Guidelines* (ISO, 2006).
70. UltraTech Cement Ltd. Environmental Product Declaration of Cement Products (EPD No. S-P-05019). The International EPD® System. https://www.environdec.com/library/epd5019. (2022).
71. Vilniaus karjerai, JSC. Environmental Product Declaration: Aggregates (EPD No. S-P-05181). The International EPD® System. https://www.environdec.com/library/epd5181. (2021).
72. Biokolprodukter AB. Environmental Product Declaration: Biochar (EPD No. S-P-12414). The International EPD® System. https://www.environdec.com/library/epd12414. (2024).
73. Sika Services AG. Environmental Product Declaration: Superplasticizers Sika® ViscoCrete®-Ultra-600 (EPD No. S-P-06999). The International EPD® System. https://www.environdec.com/library/epd6999. (2022).
74. Nienborg, B. et al. Life cycle assessment of thermal energy storage materials and components. *Energy Procedia* **155**, 111–120. https://doi.org/10.1016/j.egypro.2018.11.063 (2018).

Author contributions

Conceptualization, W.C.; methodology, W.C. and H.D.Y.; data curation, S.B.K., J.S.W. M.K.P.; writing—original draft preparation, S.B.K. and J.S.W.; writing—review and editing, H.D.Y.; Funding Acquisition, W.C. All authors have read and agreed to the published version of the manuscript.

Funding

This work was supported by a National Research Foundation of Korea grant, funded by the Korean government (MSIT). (No. RS-2024–00408370).

Declarations

Competing interests

The authors declare no competing interests.

Additional information

Correspondence and requests for materials should be addressed to H.-D.Y. or W.C.

Reprints and permissions information is available at www.nature.com/reprints.

Publisher's note Springer Nature remains neutral with regard to jurisdictional claims in published maps and institutional affiliations.